Interplay between local structure and transport properties in iron-doped $LiCoPO_4$olivines

Sergio Brutti[1,2,]*, Jessica Manzi[1], Daniele Meggiolaro[2], Francesco M. Vitucci[2], Francesco Trequattrini[2,3], Annalisa Paolone[2], Oriele Palumbo[2,]

[1]Dipartimento di Scienze, Università della Basilicata, V.le Ateneo Lucano 10, 85100 Potenza, Italia

[2]CNR-ISC, U.O.S. Sapienza, Piazzale A. Moro 5, 00185 Roma, Italia

[3]Dipartimento di Fisica, Università di Roma La Sapienza, P.le Aldo Moro 5, 00185 Roma, Italia

* corresponding author: emails sergio.brutti@unibas.it

Abstract

$LiCoPO_4$ (LCP) is a challenging high voltage positive electrode material for next generation secondary Li-ion cells. Doping the LCP olivine lattice with iron and annealing the material at high temperature disclose improved and stable performances in lithium cells. Here we investigate the structural effects of iron doping and annealing at high temperature by advanced synchrotron X-ray techniques (X-ray diffraction and absorption) in close comparison with the corresponding performances in lithium cells (lithium de-insertion/insertion) and the ionic diffusion coefficients evaluated by galvanostatic intermittent titration tests. The partial substitution of cobalt ions in the olivine lattice with iron ions, 2+ or 3+, strongly affects the long range crystal structure as well as the short range atomic coordination. These structural changes alter the concentration of antisite defects, the natural concentration of lithium vacancies, the size of the lithium diffusion channels along the [010] direction as well as their local distortion. The balancing between these competitive effects modulate the lithium transport properties in the lattice.

Keywords: $LiCoPO_4$, iron doping, XAS, XANES, EXAFS, XRD, synchrotron, GITT, lithium diffusion coefficient

1. Introduction

A breakthrough progress in Li-ion batteries (LIBs) can be achieved in terms of higher energy densities, longer cycle life, improved safety and sustainability [1] by the development of anode, cathode and electrolyte materials relying on innovative chemistries [2,3].In recent years many possible alternative formulations for next generation lithium-ion cells have been proposed in the literature, all based on a variety of different chemistries at the cathode, anode and electrolyte sides [4–6]. Among them we demonstrated the concept of a 4.4 V Li-ion cell made by coupling a $LiCo_{0.9}Fe_{0.1}PO_4$olivine(LCfP) cathode, a nanocomposite Sn-C anode and an ionic liquid-based electrolyte [7]. This formulation is an interesting alternative in respect to the analogue 4.5 V cell (e.g. [8]) based on the spinel $LiMn_{1.5}Ni_{0.5}O_4$ cathode and a carbonaceous cathode, due to the intrinsic improved safety on both the cathode (olivine vs. spinel) [9–11] and electrolyte (ILs vs organic carbonates) sides [12,13].

The $LiCoPO_4$ cathode (LCP) is a promising high potential positive electrode material for high energy Li-ion cells due to its very high working potential (>4.7 V vs. Li)[14]. Unfortunately, compared to the isostructural and commercially exploited $LiFePO_4$, LCP cathodes suffer poor reversibility in the first electrochemical de-insertion/insertion [15], a remarkable capacity fading upon cycling in lithium cells [16,17] and a spontaneous self-discharge once fully charged [18,19]. Some of these drawbacks can be mitigated by an appropriate tuning of the cathode composition, especially by partial substitution of the Co^{2+} with Fe^{2+}/Fe^{3+}.

The synthesis of LCP-based olivines with partial substitution of cobalt with iron (LCfP) has been already proposed in the literature [16,20–29]. In particular Han and co-workers [21] illustrated the beneficial effects of the Fe^{2+} doping in terms of reversibility of the electrochemical lithium de-insertion/insertion from/into the LCP olivine lattice. Similar benefits have been highlighted also by Allen and co-workers [22,27] who showed the long term cycling stability of iron-doped LCP materials and discussed the complex interplay between the structural alterations of the lattice induced by

Fe^{2+}/Fe^{3+}doping and the transport properties. Similar studies focused on the investigation of the effect of Fe^{2+}doping onto the crystal structure and electrochemical properties in lithium cells of LCfP materials have been proposed by Kang [23], Yang [24], Strobridge[25] and Kosolova[30]. In ref. [16] we showed the superior performances in lithium cells of an LCfP material obtained by solvothermal synthesis followed by high temperature annealing. Apparently the simultaneous partial substitution of cobalt with iron and thethermal treatment at high temperature in argon plays a major role in the enhancement of the reversibility of the lithium de-insertion/insertion in the LCfP lattice.

Here we illustrate in details the short and long-range structural alterations induced by iron-doping and high temperature annealing on LCP-based olivine lattice materials synthesized by a low temperaturesolvothermal method [15,31,32]. Our analysis, based on synchrotron X-ray diffraction and X-ray absorption experiments, allows to closely relate the local coordination around the transition metals with the redox activity in lithium cells as well as with the ionic transport properties obtained by Galvanostatic Intermitted Titration Tests (GITT).

2. Experimental details

2.1Synthesis route

LCP has been synthesized by a solvothermal route[15,31,32]. Two water solutions, one containing $LiOH•H_2O$ (solution A) and another containing LiH_2PO4 and $CoSO_4•7H_2O$ (solution B) have been added in sequence to ethylene glycol (EG) under vigorous stirring (EG:H_2O v/v ratio=2:1, final volume 30 ml). The molar ratios of LiH_2PO_4, $CoSO_4•7H_2O$ and $LiOH•H_2O$ have been optimized to the values 1:1:1.75. The Co^{2+} concentration in the final EG:H_2O solution is 0.1M. The obtained purple suspension has been sealed into a 45 mL Teflon-lined autoclave and heated in oven at 220°C for 15 h. The products have been filtered, washed with H_2O/ethanol and dried in oven. Iron doped materials have been obtained by using as additional reagent $FeSO_4•7H_2O$ and by setting the relative molar ratio of $CoSO_4$ and $FeSO_4$ to 0.9:0.1. The composition of the synthesized material has been

determined by inductively coupled plasma−atomic emission spectroscopy (ICP-AES) using a Vista MPX Rad−VARIAN instrument following the experimental protocol described elsewhere[16]. Undoped LCP and iron-doped LCP have been also annealed at high temperature under Ar flow (40 ml/min) at 700°C for 1h.

Four samples have been synthesized and studied: a summary of the synthesis conditions, estimated stoichiometries from ICP-AES [16] and the corresponding sample codes adopted throughout the text is presented in the table 1. The possible minor alteration of the stoichiometries for samples annealed at high temperature compared to the pristine ones has been discussed by us in ref. [16] and theseevaluationsare here adopted.

Table 1. Synthesis conditions and estimated stoichiometries .

Sample coding	**$CoSO_4$: $FeSO_4$ molar ratio**	**Annealing temperature under Ar flow /°C**	**Estimated stoichiometry from ICP-AES**
LCP	1:0	-	$Li_{1.000}Co_{1.001}PO_4$
LCP@Ar	1:0	700	$Li_{1.000}Co_{1.001-x}PO_4$
LCfP	0.9:0.1	-	$Li_{0.944}(Fe_{0.1}Co_{0.9})_{1.027}PO_4$
LCfP@Ar	0.9:0.1	700	$Li_{0.944-x}(Fe_{0.1}Co_{0.9})_{1.027}PO_4$

2.2 X-ray diffraction experiments

XRD experimentshave been carried out at the ELETTRA synchrotron radiation source (MCX beamline, X-ray wavelength = 1.24 Å). XRD has been recorded in the 12-60° 2θ range with steps of 0.015° (time/step of 2 sec). Structure refinement has been performed by the Rietveld method using GSAS[34]starting from the olivine lattices of the prototypal $LiCoPO_4$ phase (orthorhombic unit cell with space group n°62 Pnma, Li atoms in 4a (0,0,0), Co in 4c (x_{TM},¼,z_{TM}), P in 4c (x_P,¼,z_P), O in

4c (x_O,¼,z_O) 4c' ($x_{O'}$,¼,$z_{O'}$), and 8d ($x_{O''}$,$y_{O''}$,$z_{O''}$))[35]. The structure of the olivine lattice of the $LiCoPO_4$ phase is represented in the figure 1.

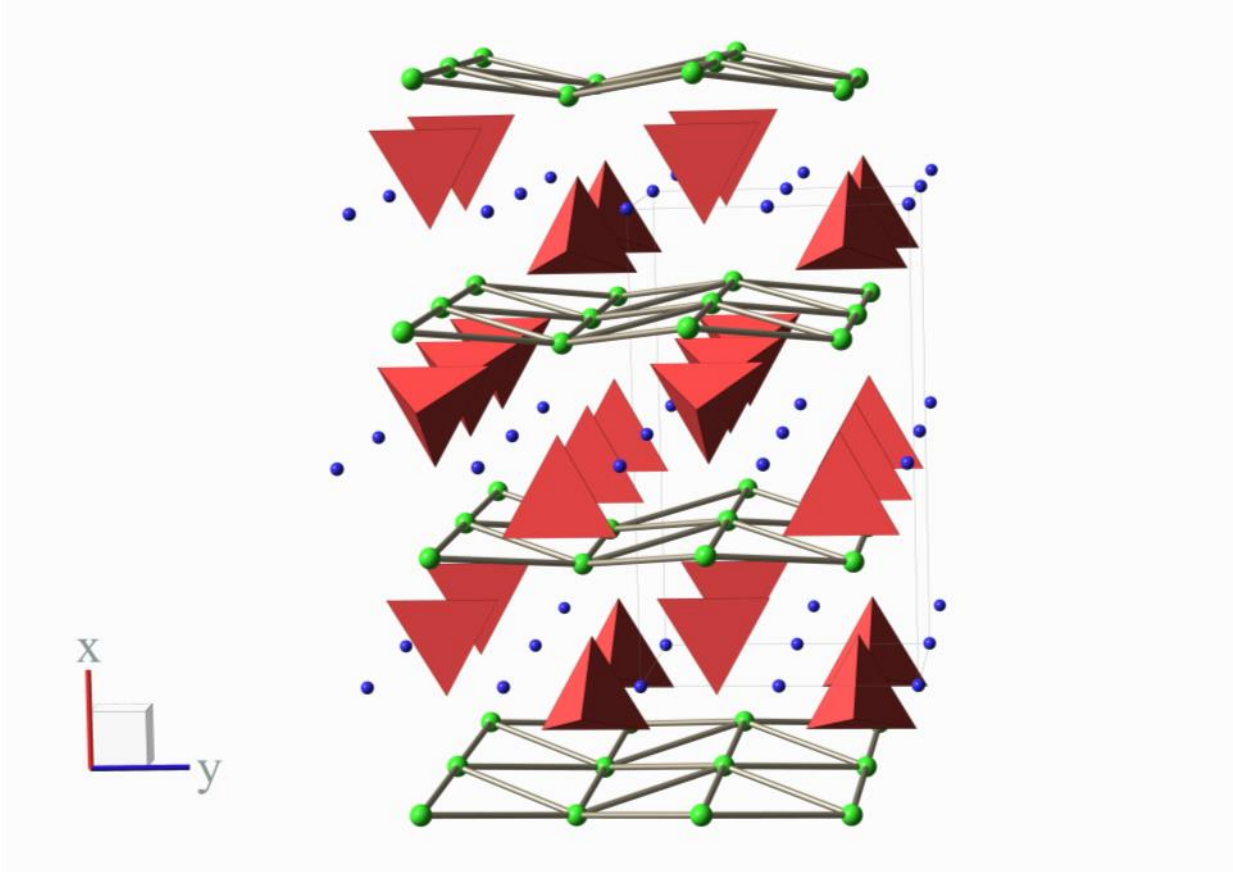

Figure 1. Structure of the olivine lattice. Green spheres are metal atoms, blue ones are lithium atoms and the PO_4octhaedra are drawn in red.

In the Rietveld refinements, few constrains have been adopted: in particular the Li:Co:P ratios have been fixed to the estimated stoichiometries (see table 1), and thus occupancies have not been freely optimized: only the anti-site Li/Co cationic disorderhas been refined. Debye-Waller factors have been optimized by applying two constrains: all cations (i.e. Li, Co, Fe) have been constrained to the same values as well as all atoms (i.e. P and O) constituting the PO_4tetrahedra. In summary, the following parameters have been optimized: (a,b,c) lattice parameters, Caglioti coefficients, Gaussian-to-Laurentian coefficients, Debye-Waller factors for cations and for PO_4tetrahedra, the Li/Co cationic disorder and the atomic positions.

2.3X-ray absorption experiments

X-ray absorption spectroscopy experiments were carried out at the Italian beamline for X-ray absorption spectroscopy (LISA)of the European Synchrotron Radiation Facility (ESRF, Grenoble). All samples were mixed with celluloseand pressed to obtain pellets, which were measured at room temperature in transmission mode at the Co K-edge(7712 eV); iron doped samples were also measuredin fluorescence mode at theFe K-edge(7112 eV). The same sample was used for spectra at both absorption edges in order to rule out spurious contributions. Energycalibrations have been carried out using Co and Fe metal foilsas a reference; standard commercial Fe_2O_3, $LiCoPO_4$ and $LiFePO_4$ samples were also measured as references for XANESanalysis.

The analysis of the XAS signals has been performed by Viperprogram[36]. The absorption spectrum below the pre-edgeregion has been fitted to a straight line while the backgroundcontribution above the postedge region has been fitted to apolynomial function. After subtraction of the fitted background,the absorption spectra have been normalized andtransformed in the k space $\chi(k)$. The k^3 weighted EXAFSoscillations, $k^3\chi(k)$, were Fourier transformed (FT) in the krange between 1.72 and 11.87$Å^{-1}$for the Coedge andbetween 2.03 and 10.25 $Å^{-1}$ for the Fe edgeusing a Hanning window function to obtain the magnitude plots of the EXAFS spectra in R-space (Å). The analysis hasbeen restricted to the firstfour FT peaks by inverse Fouriertransforming (Fourier filtering) the data in the R rangebetween 0.85and 4.85 Å(or 0.98 and4.87 Å for the Fe edge). The fit in the k-space has been performedusing standard single-scattering EXAFS formula withamplitude and phase functions generated from ab initio codeFEFF integrated in ARTEMIS (IFEFFIT package)[37].

The fitting has been performed according totwo different models (i.e. Model A and Model B) for the analyzed range. In both case eight scattering paths have been considered. The EXAFS fitting parameters for all the shells are the bond distances and the mean square relative displacements whereas the coordination numbers have been fixed as discussed in the Results. The interatomic

distances (D) used as starting points for the fit are the values by thesynchrotron diffraction experiments (see next section).

2.4Electrochemical tests

The electrode films have been deposited on an aluminium foil by doctor-blading a slurry composed of 80% of the active material (AM), 10% of PVdF-HFP (Kynar Flex 2801) and 10% of Super P carbon in tetrahydrofuran (THF, Sigma-Aldrich). The mass loading over the aluminium foil is approximately 2-3 mg cm^{-2}. All the samples have been tested in galvanostatic cycling in lithium cell in the cell potential range 3.5–5 V at 0.1C rate (1C = 167 mA g^{-1}). The galvanostatic cycling experiments have been carried out with a MTI galvanostat using ECC-STDflat cells (EL-CELL Gmbh). The cells have been prepared in an Iteco Engineering Ar-filled glovebox, by coupling the electrode under test with a lithium foil counter electrode in 1 M $LiPF_6$ ethylene carbonate/dimethylcarbonate (EC:DMC) electrolyte solution (Solvionic), soaked on a WhatmanTM glass fiber separator.Lithium diffusion coefficients have been derived from Galvanostatic Intermitted Titration tests (GITT) experiments. GITT tests have been performed by using an MTI galvanostatanECC-REFflat cellson three-electrode cells with lithium metal foils as the counter and reference electrodes. The titrations have been carried out by applying square current pulses of 17 mA/g for 30min, followed by potential relaxation steps of 30 min at the open circuit voltage. The lithium diffusion coefficients have been calculated during electrochemical de-lithiations by applying the well-known equations described in ref. [38].

3. Experimental results

3.1. X-ray diffraction

The X-XRD patterns of synthesized samples obtained by using a synchrotron source are shown in Figure 2.

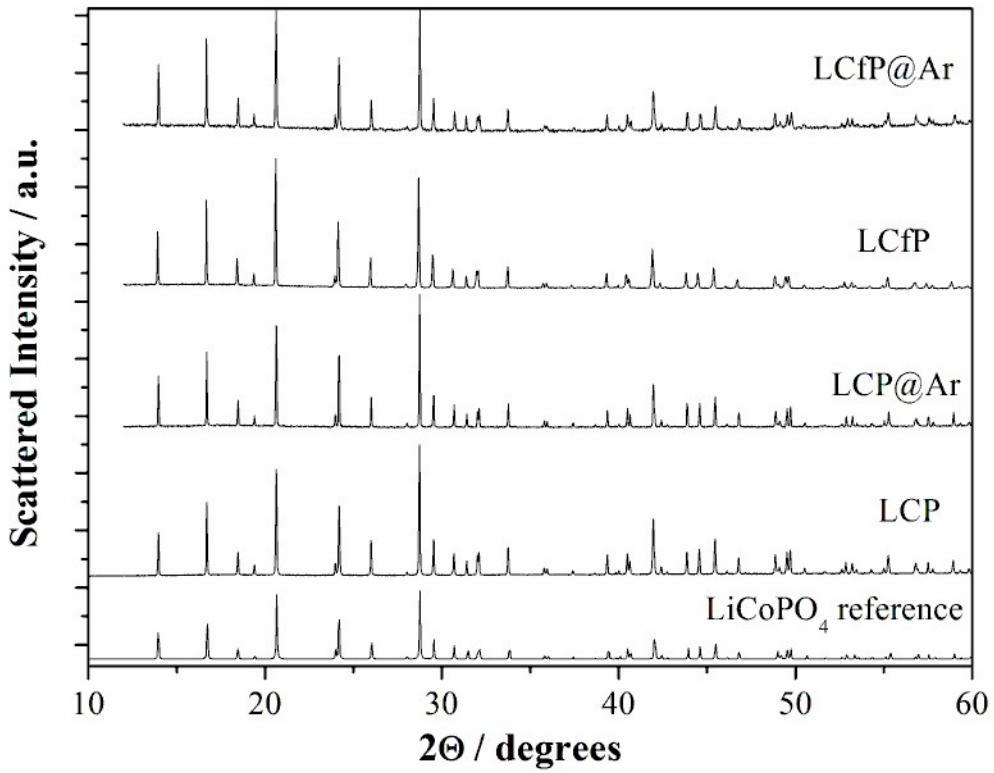

Figure 2. Synchrotron XRD patterns of the synthesized samples before and after the annealing at 700° C under Ar.

All reflections in all patterns can be indexed to single olivine phase with a *Pnma* space group. The lack of unindexed peaks confirms the phase purity of all the samples and the absence of contaminants above 2-3vol.%, which is the typical detection limit for phase identification by powder XRD [39].

Starting from the stoichiometries derived from the experimental ICP data, and summarised in the Table 1, a detailed structural analysis of all the synthesized materials has been carried out by Rietveld refinement of the diffraction data. The results of Rietveld refinement for the four materials are reported in Table 2-3-4-5.

Table 2. Summary of the Rietveld Refinement results for the LCP sample (Li/Co anti-site defects 1.5±0.2%; R_{wp} =2.05% G.o.f. = 1.14). Errors on the last digit of the optimized atomic positions (cell axes fractions) are reported in parenthesis.

Cell parameters	Atoms	Wyckoff position	Atomic coordinates x , y , z	Debye-Waller factors / A^2	Occupancies
a=10.219±0.002	Li	4a	0 , 0 , 0	1.2±0.8	1.0
b=5.926±0.002	Co	4c	0.777(2) , ¼ , 0.522(1)	1.2±0.3	1.0
c=4.707±0.004	P	4c	0.597(2) , ¼ , 0.083(3)	0.8±0.2	1.0
	O_1	4c	0.596(1) , ¼ , 0.763(1)	0.8±0.1	1.0
	O_2	4c	0.954(2) , ¼ , 0.292(4)	0.8±0.1	1.0
	O_3	8d	0.165(3) , 0.044(4) , 0.252(2)	0.8±0.2	1.0

Table 3. Summary of the Rietveld Refinement results for the LCP@Ar samples (Li/Co anti-site defects 0.6±0.2%; R_{wp} =2.50% G.o.f. = 1.22). Errors on the last digit of the optimized atomic positions (cell axes fractions) are reported in parenthesis.

Cell parameters	Atoms	Wyckoff position	Atomic coordinates x , y , z	Debye-Waller factors / A^2	Occupancies
a=10.207±0.003	Li	4a	0 , 0 , 0	0.6±0.3	1.0
b=5.923±0.001	Co	4c	0.779(2) , ¼ , 0.522(1)	0.6±0.3	1.0
c=4.702±0.003	P	4c	0.594(2) , ¼ , 0.081(3)	0.5±0.3	1.0
	O_1	4c	0.598(1) , ¼ , 0.762(1)	0.5±0.3	1.0
	O_2	4c	0.954(2) , ¼ , 0.292(4)	0.5±0.3	1.0
	O_3	8d	0.164(3) , 0.048(4) , 0.281(2)	0.5±0.3	1.0

In the case of LCP and LCP@Arundoped samples, the structural analyses highlight an isotropic slight contraction of the cell parametersand the corresponding shrinking of the unit cell volume (-0.3%) after annealing. This cell volume contraction occurs with simultaneous fading of the refined Li/Co anti-site defects. This combined trend of the cell volume and cationic disorder has been already reported by us for similar LCP samples [3216] as well as for the parent $LiFePO_4$ lattice[40].

Table 4. Summary of the Rietveld Refinement results for theLCfP sample (Li/Co anti-site defects 2.1±0.4%; R_{wp} =2.87% G.o.f. = 1.42). Errors on the last digit of the optimized atomic positions (cell axes fractions) are reported in parenthesis.

Cell parameters	Atoms	Wyckoff position	Atomic coordinates x , y , z	Debye-Waller factors / A^2	Occupancies
a=10.224±0.003	Li	4a	0 , 0 , 0	1.2±0.3	1.0
b=5.930±0.001	Co	4c	0.779(2) , ¼ , 0.520(1)	1.2±0.3	0.9
c=4.704±0.003	Fe	4c	0.779(2) , ¼ , 0.520(1)	1.2±0.3	0.1
	P	4c	0.594(2) , ¼ , 0.082(3)	0.6±0.3	1.0
	O_1	4c	0.600(1) , ¼ , 0.758(1)	0.6±0.3	1.0
	O_2	4c	0.956(2) , ¼ , 0.299(4)	0.6±0.3	1.0
	O_3	8d	0.167(3) , 0.046(4) , 0.283(2)	0.6±0.3	

Table 5. Summary of the Rietveld Refinement results for theLCfP@Ar sample (Li/Co anti-site defects 0.7±0.2%; R_{wp} =3.38% G.o.f. = 1.81). Errors on the last digit of the optimized atomic positions (cell axes fractions) are reported in parenthesis.

Cell parameters	Atoms	Wyckoff position	Atomic coordinates x , y , z	Debye-Waller factors / A^2	Occupancies
a=10.191±0.003	Li	4a	0 , 0 , 0	0.8±0.3	1.0
b=5.919±0.001	Co	4c	0.778(2) , ¼ , 0.522(1)	0.8±0.3	0.9
c=4.705±0.003	Fe	4c	0.778(2) , ¼ , 0.522(1)	0.8±0.3	0.1
	P	4c	0.594(2) , ¼ , 0.086(3)	0.7±0.3	1.0
	O_1	4c	0.601(1) , ¼ , 0.761(1)	0.7±0.3	1.0
	O_2	4c	0.953(2) , ¼ , 0.304(4)	0.7±0.3	1.0
	O_3	8d	0.166(3) , 0.049(4) , 0.284(2)	0.7±0.3	1.0

Turning to the doped LCfP sample, the iron substitution slightly increases anisotropically the cell volume of + 0.1% compared to the undoped LCP sample (+0.1% along the *a* and *b* axes and -0.1% along the *c*-axis). This minor expansion is expected since the Fe^{2+} ionic radius (0.780 Å) is

slightly larger in respect to Co^{2+} (0.745 Å) [41], and confirms our findings on similar samples prepared in slightly different experimental conditions [16].

For what concerns the LCfP@Arsample, it shows a remarkable contraction of the cell volume (-0.5%) after annealing, in comparison to the pristine LCfP sample. This volumetric contraction is anisotropic since the *a* and *b* cell parameters decrease of -0.3% and -0.2%, respectively, whereas the *c* cell parameter is unaltered. Also in this case, the cell shrinking occurs in parallel with a decrease of the antisite cationic disorder.

Starting from the structural results from the Rietveld refinements some additional comments can be done concerning the changes of the bond distances around the metals in the octahedral site (i.e. 4c site). In the table 6, bond distances estimated from structural refinements of the XRD data are summarized.

Table 6. Bond distances (Å, estimated mean uncertainty ±0.01Å) and degeneracies (in parentheses) calculated from structural refinements of the synchrotron XRD data (M=Co for LCP and CPD@Ar, M=Co/Fe for LCfP and LCfP@Ar)

Chemical bond	LCP	LCP@Ar	LCfP	LCfP@Ar
M-O	2.06 (x2)	2.08 (x2)	2.06 (x2)	2.05 (x2)
	2.09	2.09	2.09	2.07
	2.17	2.16	2.14	2.12
	2.20 (x2)	2.19 (x2)	2.19 (x2)	2.20 (x2)
mean	2.13	2.13	2.12	2.12
M-P	2.79	2.80	2.79	2.78
M-Li	3.21	3.21	3.21	3.20

Apparently the four samples show only minor changes of the bond distances. However, one can note that the metal-oxygen bond distances decrease with iron doping and become even smaller after annealing.It is important to underline that in the doped samples, the estimated bond distances M-O are unavoidably weighted means that include both the Co-O and the Fe-O first coordination

shells. In this view the XRD technique is unable to finely decouple the possible alteration around the cobalt or the iron ions in the olivine lattice. More details about the local structure of the four samples around the transition metals can be obtained by the XAS analysis (see below).

In summary XRD confirms that all samples are constituted by pure olivine structure and that doping affects the long-range ordering of the lattice. The high temperature annealing under Ar leads to the cell contraction and to an antisite defect concentration decrease. However, in the undopedLCP@Ar sample the volumetric contraction is isotropic whereas in the LCfP@Ar is anisotropic.

3.2. X-ray absorption: XANES

The Co K-edge and Fe K-edge data are presented in the figure 3a-b. For each spectrum, the intensity of the main absorption peak has been normalized at the peak maximum and samples compared using E_0, defined as the energy at half the height of this absorption peak [42]. The standards used for energy calibrationcontained Co^0, Co^{2+}, Fe^{2+} and Fe^{3+}.

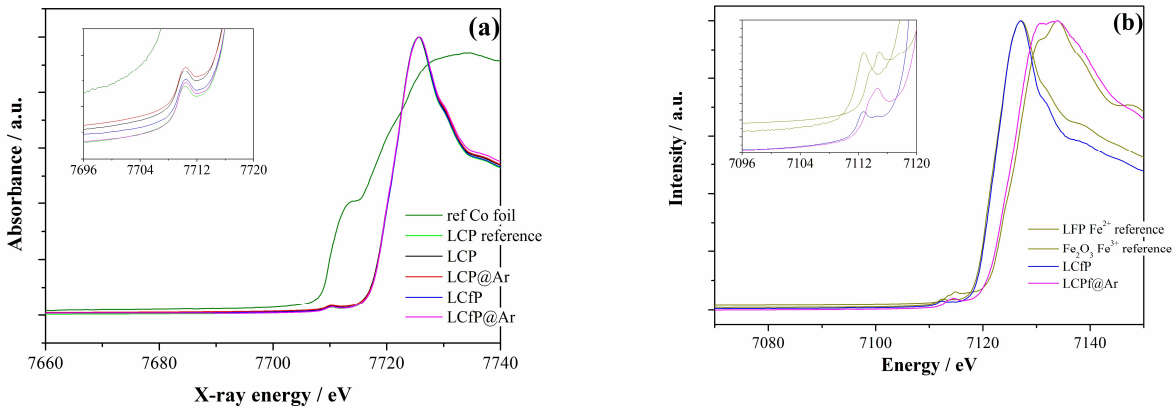

Figure 3. XANES (a) Co K-edge and (b) Fe K-edge for the four synthesized samples. In the inset the pre-edge regions are shown.

In Figure 3a, all the Co edges reveal the Co 1s→4p white lines that are apparently unaltered regardless the eventual iron-doping or annealing at high temperature. The dipole forbidden pre-edge

peaks, attributable to the Co 1s→3d transition, follow an identical trend compared to the white line, thus indicating the retention of the Co^{2+} state seen in the calibration standard [23]. On the contrary in the figure 3b, both Fe pre-edge and E_0, suggest a 2+ oxidation state for the LCfP sample and an almost 3+ state for the LCfP@Ar after annealing. The estimated iron oxidation state in the LCfP@Ar sample is 2.8±0.1.

The experimental evidence of the iron oxidation of the LCfP lattice after the high temperature annealing confirms our hypothesis discussed in ref. [16], as well as the observation by Allen and co-workers by Mossbauer spectroscopy for an iron doped $LiCoPO_4$sample annealed at 600°C in nitrogen flow [22].

3.3. X-ray absorption: EXAFS

The obtained radial distribution functions for the four samples are shown in Figure4 for both the Co- (upper panel) and Fe-edges (lower panel).

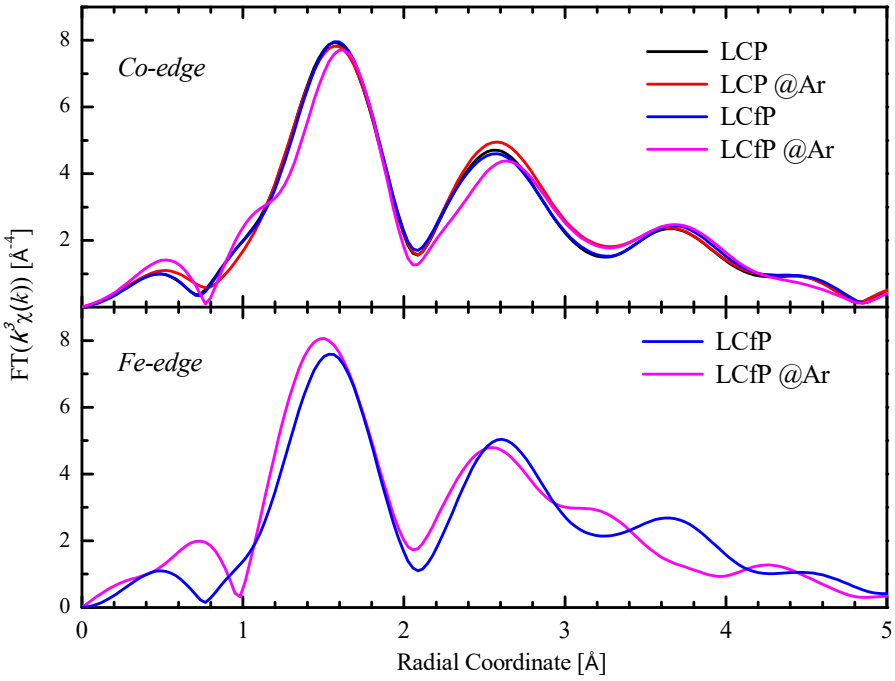

Figure 4. Radial distribution function obtained after Fouriertransformation of $k^3\chi(k)$

Both Co and on the Fe-edges show a strong peak between 1 and 2 Å, and three additional peaks at higher distances, in the range between 2 and 5 Å, whose intensity decreases with increasing distance. All the plotted radial structures present similar shape, suggesting a similar local structure around both the scattering atoms, i.e. Fe and Co, in all the four samples. Small differences can be noted in the radial function of the LCfP@Ar sample at the Co-edge (around 1.2 Å) and more clearly at the Fe-edge, where a shift in the peak position centred between 3 and 4 Å is evident.

Inanalogy with the EXAFS analyses of the isostructural LiFePO4 phase [43,44], the only previous EXAFS study on $LiCoPO_4$ by Kang and co-workers assign the first three peaksof the radial distribution function to the Co-O, Co-P and Co-Co bonds, respectively[45]. In particular Kang performed a quantitative EXAFS fit of the Co-O peak using four different Co-O distances[44], two of them with a double degeneracy, to mimic the CoO_6 octahedral coordination. On the other hand,for the isostructural $LiFePO_4$ phase excellent fits have beenrefined assuming only three Fe-O distances, all with a double degeneracy[43],with negligible improvements obtained from an additional fourth Fe-O component. Turning to the higher shells, quantitative EXAFS fittings performed only on the isostructural $LiFePO_4$ phase assumed five phosphorous atoms located at three different distances and outer iron neighbors at two different distances [43,44].

As previously stated, we assumed two models, namely Model A and B.InModel A (see the supplementary material) six oxygen atoms, located at three different distances, constitute the first neighbors shell. The second neighbors shell has been modeled with five phosphorous located at two different distances and six oxygen atoms located at a slightly higher distance.The third shell at higher distances is due to Co/Fe atoms at two different distances.In particular we assumed 4 metal atoms at a shorter distance (~ 3.9 Å) from the scattering center and two at longer distance (~ 4.6 Å). This assumption came from simple considerations from the crystal structure shown in the Figure1.

In order to check the reliability of the Model A, we also considered Model B (see the supplementary material) that matches the assumption made for the isostructural $LiFePO_4$ in ref. [43]. In particular Model B adopts the same contributions for the first (oxygen) and the third (metal) shell

compared to Model A, but considering different contributions for the second shell. In particular in Model B, the second neighbors shell has been modeled with five phosphorous located at three different distances, thus neglecting the contribution of the six oxygen atoms located at a slightly higher distance.

It is important to underline that the Model B is close to other models previously reported in literature for the EXAFS analysis [43,44,46]of the $LiFePO_4$ olivine structure. However, an accurate evaluation of all the possible scattering paths obtained from the ab initio code FEFF integrated in ARTEMIS [37] suggests the occurrence of significant contribution due to scattering from the six second-neighbors oxygen, thus making Model A closer to the crystallographic structure.

The analysis has been carried out for both models, obtaining qualitatively similar results: the relative quality of the various fitting has been evaluated by using the usual R factor [37].The EXAFS fitting parameters for all the shells are: (a) the bond distances and (b) the mean square relative displacements, whereas the coordination numbers have been fixed. The number of fitting parameters are the same for the two models. In the following we describe the results from Model A, which provided the smallest R factor values for all fits, whereas those of Model B are summarized in the supporting material.

Quantitative fittinganalyseshavebeenperformedonthe curves oftheinverseFourier transformation in the *k* range accordingtothe peaksappearingintheradialstructure functions and are plotted in the Figure5 for both models. The fitted distances between scattering atoms for the Model A are summarized in Table 7 whereas the mean square relative displacements are reported in the supplementary material.

It must be noticed that both models provides for the first coordination shell distances which are slightly lower than the shortest metal–oxygen distances calculated from the Rietveld refinements (1.85-1.93 vs 2.05-2.08 Å). A similar discrepancy for the shortest metal oxygen distances has been already observed for EXAFS and XRD results on $LiFePO_4$ [44].

The bond distances in the first Co-O coordination shell (data measured at the Co k-edge) show minor variations. The Co-O mean distances in the undoped olivines slightly expands after annealing. Also the distortion of the CoO_6octahedraslightly increases after the annealing being the three fitted distances scattered in a larger interval, i.e. 1.93-2.17 vs 1.92-2.19Å for the LCP and LCP@Ar samples, respectively. On the contrary doping with Fe^{2+} leads in the LCfP sample to a small contraction of the mean Co-O distance compared to the undoped LCP lattice, and to an apparent negligible effect on the octahedral distortion. After annealing under Ar the LCfP@A sample undergoes the observed oxidation of Fe^{2+} to Fe^{3+} (see the previous section) and to a slight contraction the CoO_6octahedra.

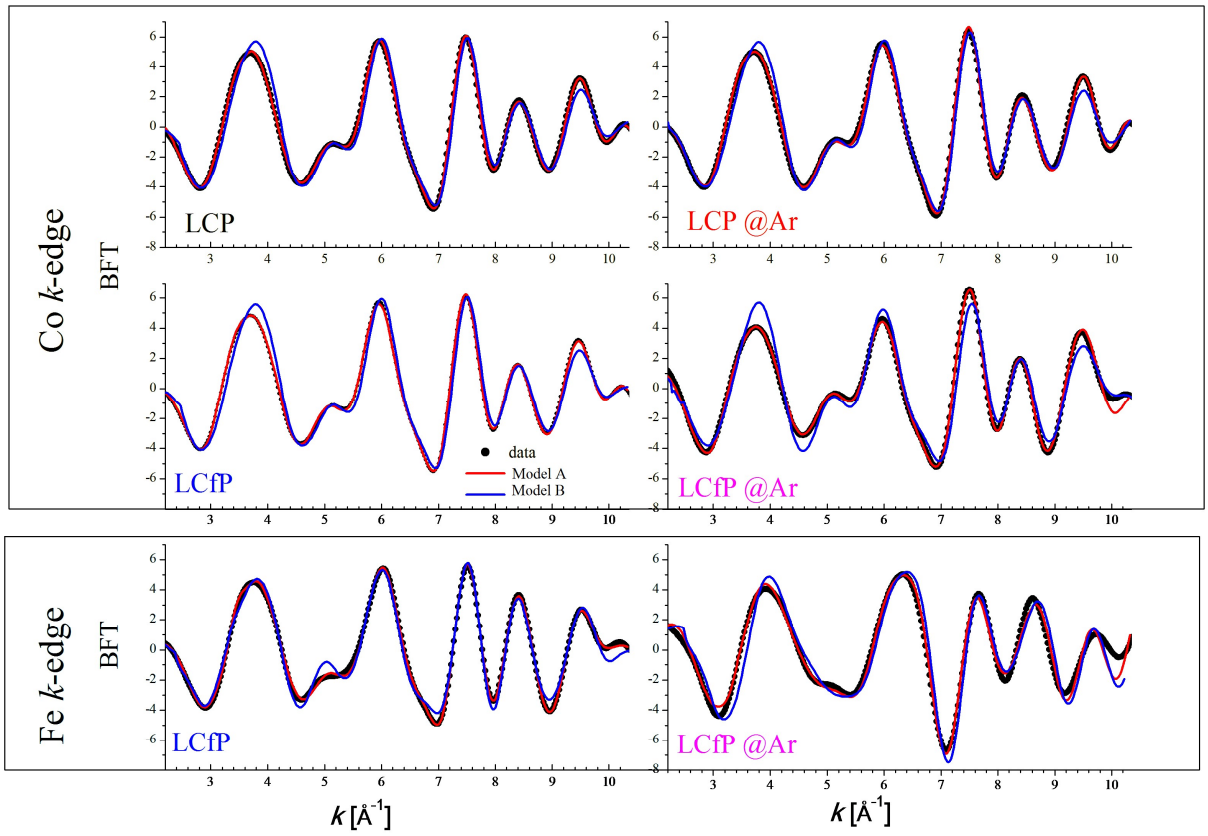

Figure 5. Data (point) and best fit (red line = Model A; blue line = Model B) for the BFT of the k^3-weighted Co and Fe K-edge signal for samples LCP, LCP@Ar, LCfP and LCfP@argon.

Turning to first Fe-O coordination shell in the LCfP sample, the FeO_6octahedra show similar distances and distortion compared to the CoO_6octahedra. After annealing in Ar, i.e.inLCfP@Ar

sample, the Fe-O first coordination shell shrinks and the octahedral distortion around the iron centres decreases, being the Fe-O distances scattered in a narrower interval compared to the CoO_6octahedra, i.e. 1.85-2.16 vs 1.88-2.11Å for the LCfP@Ar and LCfP samples, respectively.

Table 7. FeFF fit results (distances between scattering atoms in Å) for the Model A for the four considered samples. CN is the coordination number; M-Z represent the central absorber (M, that is Co or Fe respectively in the Co K-edge and the Fe K-edge fits) and the scattering atom (Z, that is O, P/O or Co/Fe in the three shells considered). Statistical errors on distances are in all cases smaller than 0.01 Å.

			Co K-edge				Fe K-edge	
Shell	M-Z	CN	LCP	LCP@Ar	LCfP	LCfP@Ar	LCfP	LCfP@Ar
1st	M-O	2	1.93	1.92	1.91	1.85	1.92	1.88
	M-O	2	2.02	2.03	2.02	2.02	2.00	1.97
	M-O	2	2.17	2.19	2.17	2.16	2.17	2.11
2nd	M-P	1	2.82	2.78	2.80	2.87	2.83	2.73
	M-P	4	3.28	3.25	3.26	3.27	3.29	3.25
	M-O	6	3.51	3.56	3.57	3.52	3.30	3.28
3rd	M-M’	4	3.86	3.85	3.88	3.85	3.97	3.41
	M-M’	2	4.74	4.72	4.76	4.76	4.86	4.33
R factor (%)			2.9	5.1	3.9	5.8	6	8.5

In summary, the simultaneous iron doping and annealing in Ar, and the consequent iron oxidation, leads to a remarkable contraction of both the Co-O and Fe-O first shells and to a decrease of the octahedral distortion. On the contrary the simple annealing under Ar of the undoped LCP leads to an additional expansion and distortion of the CoO_6octahedra, whereas the simple doping with Fe^{2+} leads to a smaller M-O distances but to an increase of the MO_6 distortion.

Compared to the pristine LCP lattice, the Co-P mean distances are larger in all the LCP@Ar, LCfP and LCfP@Ar samples. On the contrary the Fe-P mean distance is larger in the LCfP sample compared to the Co-P distance in the LCP lattice, but remarkablyshorter after annealing under Ar.

Apparently in the doped and annealed sample LCfP@Ar the PO_4octahedra shifts within the cell closer to the Fe^{3+} centers in respect to the Co^{2+} ions. This effect is expected due to the stronger Coulombian attraction of the Fe^{3+} compared to the Co^{2+} centers and to the possible occurrence of a lithium vacancy close to the Fe^{3+} ions.

Turning to the M-M' third shell distances, these values are closely related to the variation in size of the unit cell. In fact, taking into consideration the crystal structure shown in figure 4, the first Co-M (or Fe-M) distance corresponds to approximately $\sqrt{\left(\frac{b}{2}\right)^2 + \left(\frac{c}{2}\right)^2}$, where b and c are the olivine cell parameters, whereas the second Co-M (or Fe-M) distance exactly corresponds to the cell parameter c. As expected, the trend of the fitted Co-M and Fe-M third shell distances nice compares with the variation in size of the crystallographic unit cell obtained by the XRD data (see above).

The LCP@Ar sample shows a slight contraction of the Co-Co distances compared to the LCP material in parallel with the isotropic cell volume shrinking of -0.3%. The LCfP sample shows a slight enlargement of the Co-Co distances compared to the LCP sample whereas the Fe-Fe distances are approximately 2% larger compared to the Co-Co ones in the same sample. This distance expansion compares well with the overall isotropic cell volume enlargement of +0.1% and illustrates an interesting inequivalent local environment around Fe or Co.

The LCfP@Ar materials shows, in line with the overall -0.5% cell volume shrinking observed by XRD, a contraction of both the Co-M and Fe-M distances, compared to the LCfP sample. However, the Co-M and Fe-M distances vary with different magnitudes. In fact, whereas the Co-M distances in the LCfP@Ar sample decreasesless than 1% compared to the LCfP material, the Fe-M distances decreases of approximately 15%. This remarkable structural alteration is in line with the previous evidences for the Fe-O and Fe-P coordination shells and confirms the structural diversity of the local coordination around Fe or Co in the LCfP@Ar lattice.

In summary, the doping with Fe^{2+} of the olivine lattice, i.e. LCfP sample, leads to a slight overall lattice expansion as well as to a minor enlargement of the CoO_6octahedra. Moreover, despite few minor difference, all the three fitted neighbors shells around the Fe^{2+} and the Co^{2+} centers are very similar. On the contrary in the doped and annealed sample LCfP@Ar, both the FeO_6 and the CoO_6 octahedra compress, the PO_4octahedra shifts closer to the Fe^{3+} centers and overall local environment around the iron ions shrinks more remarkably compared to the analogue compression around the cobalt centers.

Despite minor differences, a comparison of the obtained parameters (see supporting info) shows that both model A and B provides the same indications about the alterations of the Co-X and Fe-X (X=O, P, M) distances in all samples.

3.4 Electrochemical data

The performances in galvanostatic tests at 0.1C rate (1C = 167 mA g^{-1}) of lithium cells using the four samples are presented in the Figure 6a-b.

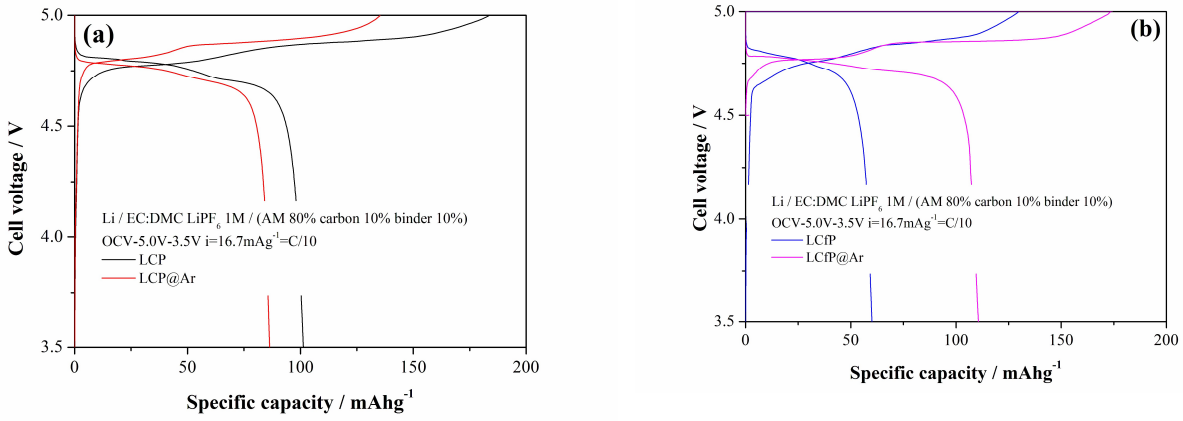

Figure 6. Cell voltage profile in galvanostatic conditions of the (a) undoped and (b) iron doped samples before and after the annealing at 700° C under Ar.

The charge/discharge profiles of the first cycles of all samples present a reversible double voltage plateau centred around 4.8 V corresponding to the redox couple Co^{3+}/Co^{2+}.The double

plateaux are due to the two consecutive biphasic electrochemical lithium extraction-insertion in the olivine lattice[35]:

$$LiCoPO_4 \leftrightarrow Li_{0.7}CoPO_4 + 0.3\ Li^+ + 0.3\ e^- \qquad [R1]$$

$$Li_{0.7}CoPO_4 \leftrightarrow CoPO_4 + 0.7\ Li^+ + 0.7\ e^- \qquad [R2]$$

Apparently the voltage profile in the first galvanostatic cycle of the doped samples shows similar features compared to the undoped ones. In all cases no evidence of a voltage plateau at about 3.4-3.6 V vs. Li^+/Li due to the Fe^{3+}/Fe^{2+} couple during the first charge has been recorded. This peculiar electrochemical feature has been already observed in the literature on similar iron-doped lithium cobalt phosphate materials [21–24,30].

The galvanostatic response of LCP@Ar reveals a negative effect of the high-temperature annealing on the cell performances: it shows reversible voltage plateaus centred at 4.8 V, with a discharge capacity through the first cycle of about 85 mAh g^{-1}compared to the 103 $mAhg^{-1}$ of the LCP material. On the contrary the iron-doped sample boosts its electrochemical reversibility after the high temperature annealing. The LCfP@Ar sample shows a similar galvanostatic plateau at 4.8 V, with a reversible capacity that exceeds 110 mAh g^{-1}, overcoming the performances of LCfP and of the undoped LCP samples. Also in the case of the LCfP@Ar sample no evidence of electrochemical processes associated to the Fe^{3+}/Fe^{2+} redox couple within the voltage range 3.4-3.6 Vis observed. This absence is not surprising, since we proved by XANES the oxidation of Fe^{2+} during annealing (see the previous section).

The lithium diffusion coefficients in all samples have been evaluated by GITT in order to highlight differences and trends induced by doping and annealing. The experimental results obtained as mean values between charge and discharge data in two different GITT experiments are shown in the figure 7as a function of the nominal lithium content (x) in the olivine lattice (Li_xMPO_4 with M=Co or Co/Fe).

The lithium diffusion coefficients range for all samples between 10^{-15} and 10^{-10} cm^2s^{-1} and show similar trends with the lithium content. These values are in line with the data measured by Allen[27], Kang[45], Kosova and co-workers[26] by impedance spectroscopy, chrono amperometry and GITT, respectively, for the $LiCoPO_4$ and $LiCo_{1-x}Fe_xPO_4$ (x=0.1[27], 0.05[23] and 0.5[26]).

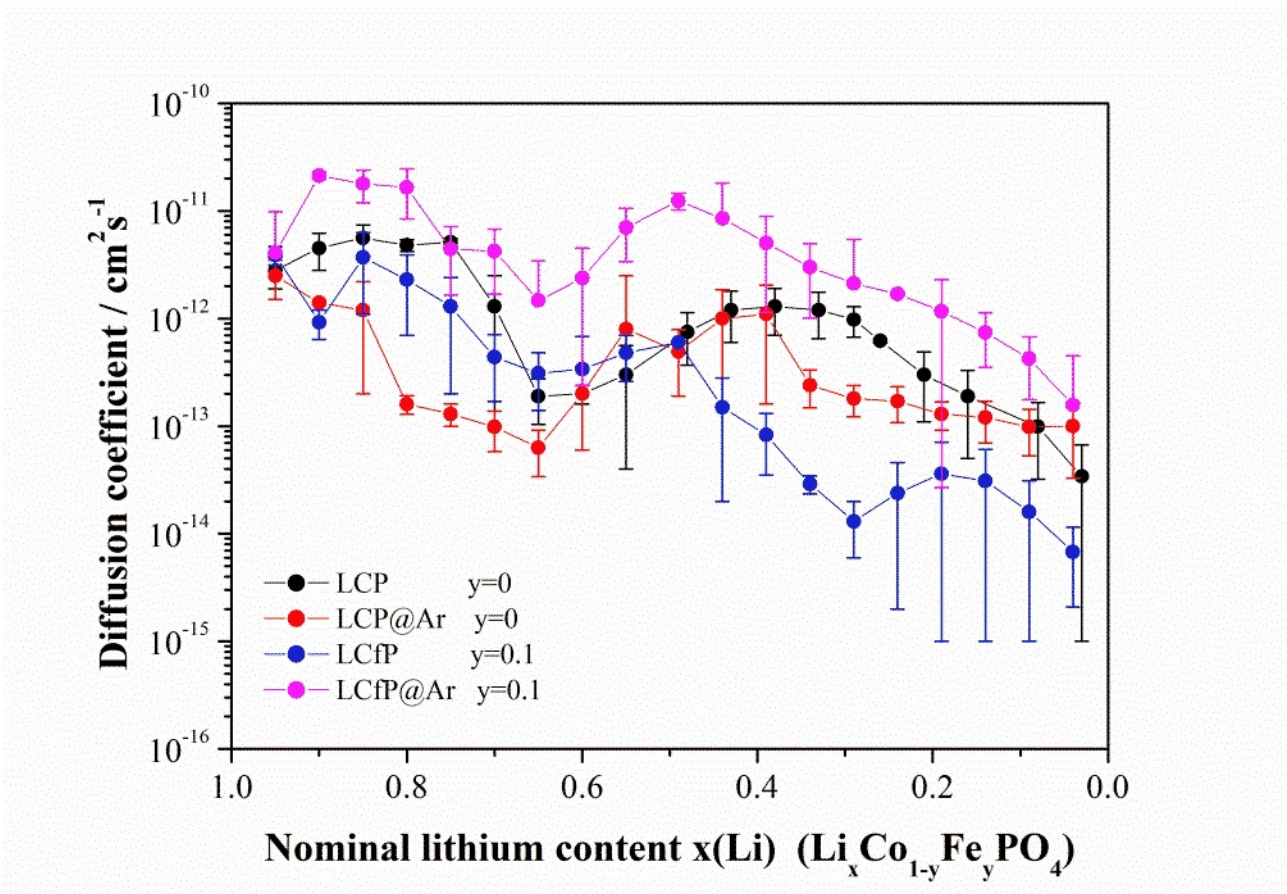

Figure 7.Li^+ diffusion coefficients for the undoped and iron-doped samples before and after the annealing at 700° C inAr derived from GITT runs.

Turning to the evolution of the ionic diffusion coefficients with the lithium content, a first decreasing slope is observed between the x=1 and x=0.65 followed by a slight increase to a pseudo-maximum at x=0.5-0.45. At smaller lithium content the lithium diffusion coefficient fades almost monotonically in all cases. However the magnitude of the various trends is different in the various samples. The high temperature annealing negatively affects the lithium mobility in the undoped sample, as the LCP@Ar sample shows a diffusion coefficient systematically smaller compared to

the LCP one. Similarly the iron doping damages the dynamics of lithium in the lattice: at lithium content x<0.5, the LCfP sample shows the smallest diffusion coefficients among all samples.

Apparently the simultaneous iron doping and annealing leads to an improved lithium mobility compared to the pristine undoped LCP samples. In fact the LCfP@Ar sample shown the largest diffusion coefficients among all samples in the entire composition range. It is interesting to observe that the ratio between the ionic diffusion coefficient between the undoped LCP and the doped and annealed LCfP@Ar sample, i.e. $D_{LCP}^{Li^+} / D_{LCfP@Ar}^{Li^+}$, ranges approximately between 0.2 and 0.5, being the lithium ions two to five times more mobile in the LCfP@Ar samples compared to the benchmark LCP. This difference is in agreement with the ratio (approximately 0.4) in the diffusion coefficient estimated by Allen and co-workers by impedance spectroscopy on the same stoichiometries and pristine iron oxidation state.[27]

4. Discussion and conclusions

The XRD and XAS data analyses of the four LCP-based olivine materials highlight a complex alteration of the local coordination environment around the transition metals as well as a parallel modification of the long range ordering due to iron doping and annealing in argon at 700°C. Moreover these four materials show different functional properties in lithium cells in terms of reversible lithium electrochemical de-insertion/insertion as well as lithium ionic diffusivity. Having in mind that the reversibility of lithium extraction/insertion in galvanostatic tests can be strongly affected by the ionic transport properties, it is therefore important to decouple and discuss the various effects that drive the interplay between structure and lithium mobility.

Atomistic simulations and energetic evaluation of the diffusion of lithium ions in the LiFePO4 olivine lattice have been proposed and discussed by many research groups. [47,48]The lowest energy migration pathway for vacancy hopping between neighbouring lithium positions is along the Li-ion channels in the [010] direction. The size of these channels, the thermodynamic concentration

of lithium vacancies in the lattice as well as the presence of cation mixing on the lithium atomic sites (antisite defects) play a major role in the enhancement of the lithium mobility [40,47–49].

To facilitate the discussion a pictorial representation of the alteration of the structure along the [010] lithium diffusion paths in the four samples is shown in the figure 8.

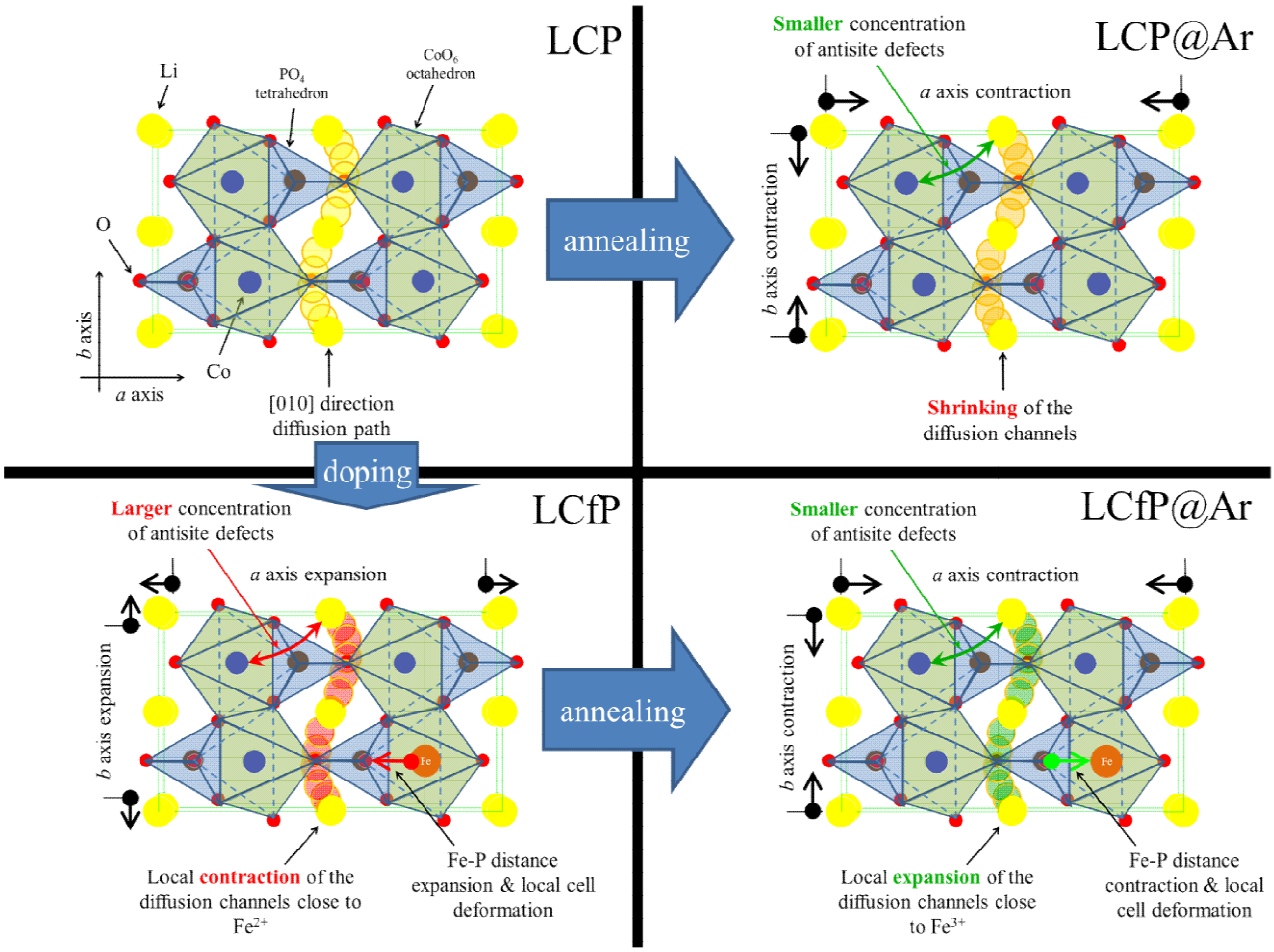

Figure 8. Pictorial representation of the alteration of the structure along the [010] lithium diffusion paths in the four samples.

Assuming the LCP sample as benchmark, the annealing under Ar to give the LCP@Ar sample results in the crystallographic cell contraction without remarkable alterations in the local coordination around the cobalt ions. This structural evolution leads to the shrinking of the size of the lithium channels along the [010] direction in line with the decrease of the concentration of

antisite defects predicted by the Rietveld Refinement. Apparently these two effects counterbalance, thus resulting in a slightly smaller ionic diffusion coefficient.

The partial substitution of cobalt with Fe^{2+} ions in the LCfP sample leads to a cell expansion,mainly along the *a* and *b* axes, as well as to the slight shift of the PO_4 octahedron far from the iron centres and closer to cobalt. These structural changes results in the overall expansion of the size of the lithium channels in proximity of cobalt ions and justify the increase of the concentration of antisite defects estimated in the Rietveld Refinments. The different coordination around the two transition metal ions may also suggest the possible occurrence of diffusion bottlenecks in proximity of iron centres due to the shift of the phosphate ion tetrahedra. The resulting overall effect is a remarkable decrease of the mobility of lithium ions in the LCfP material compared to the LCP.

The annealing under Ar of the LCfP sample to give the LCfP@Ar material leads to: (a) the almost full oxidation of the Fe^{2+} to Fe^{3+}, (b) a remarkable cell shrinking and (c) the shift of the PO_4 octahedron closer to the iron ions. These effects leads to the contraction in size of the lithium channels along the [010] direction and support the parallel decrease of the concentration of antisite defects estimated by the Rietveld Refinements of the XRD data. Contrary to the case of the LCfP sample, the different coordination around the two transition metal ions may also lead to a further local enlargement of the lithium diffusion in proximity of iron centres due to the opposite shift of the phosphate ion tetrahedral closer to the metal center. Moreover, the oxidation of the iron ions is expected to increase the natural concentration of lithium vacancies, as already discussed by us in ref. [16].All these concomitant effects result in the increase of the diffusion coefficient of lithium ions in the LCfP@Ar material compared to the LCP.

In summary the partial substitution of cobalt ions in the olivine lattice with iron ions, 2+ or 3+, strongly affects the long range crystal structure as well as the short range atomic coordination. These structural changes alters the concentration of antisite defects, the natural concentration of

lithium vacancies, the size of the lithium diffusion channels along the [010] direction as well as their local distortion. The balancing between these competitive effects modulate the lithium transport properties in the lattice. In particular the incorporation in the olivine lattice of aliovalentFe^{3+} ions in the LCfP@Ar material leads to an enhancement of the lithium diffusion coefficient and to an increase of electrochemical lithium extraction/insertion reversibility in lithium cells.

Supplementary material

In the supplementary material the structure EXAFS fitting models A and B are summarized and the fitting results for Model A (mean square displacements) and B (distances and mean square displacement) are reported.

Acknowledgments

Thanks are due to the Basilicata Innovazione project for the financial support through the specific program "ValidazionedeirisultatidellaRicerca - Progetto di Convalida 2013-2014 - Synthesis of a novel $LiCoPO_4$ based composite material and testing in secondary lithium cells".
The synchrotron XRD experiments have been carried out at the MCX beamline in ELETTRA within the frame of the project 20130017 "Diffraction study of the self-discharge phenomena of $LiCoPO_4$ in rechargeable lithium cells". Thanks are due to Dr. Jasper Plaisier for the kind support.
The synchrotron XAS experiments have been carried out atLISA beamline of the European Synchrotron Radiation Facility (ESRF, Grenoble) 08-01 958 project (2014).

Bibliography

(1) Larcher, D.; Tarascon, J.-M. Towards Greener and More Sustainable Batteries for Electrical Energy Storage. *Nat. Chem.***2014**, *7* (1), 19–29.

(2) Hassoun, J.; Scrosati, B. Review—Advances in Anode and Electrolyte Materials for the

Progress of Lithium-Ion and beyond Lithium-Ion Batteries. *J. Electrochem. Soc.***2015**, *162* (14), A2582–A2588.

(3) Kraytsberg, A.; Ein-Eli, Y.; Kraytsberg, A.; Ein-Eli, Y. Higher, Stronger, Better ... A Review of 5 Volt Cathode Materials for Advanced Lithium-Ion Batteries. *Adv. Energy Mater.***2012**, *2* (8), 922–939.

(4) Hassoun, J. .; Lee, K.-S. .; Sun, Y.-K. .; Scrosati, B. . b b. An Advanced Lithium Ion Battery Based on High Performance Electrode Materials. *J. Am. Chem. Soc.***2011**, *133* (9), 3139–3143.

(5) Jung, H.-G.; Jang, M. W.; Hassoun, J.; Sun, Y.-K.; Scrosati, B. A High-Rate Long-Life Li4Ti5O12/Li[Ni0.45Co0.1Mn1.45]O4 Lithium-Ion Battery. *Nat. Commun.***2011**, *2*, 516.

(6) Di Lecce, D.; Fasciani, C.; Scrosati, B.; Hassoun, J. A Gel-Polymer Sn-C/LiMn0.5Fe0.5PO4 Battery Using a Fluorine-Free Salt. *ACS Appl. Mater. Interfaces***2015**, *7* (38), 21198–21207.

(7) Di Lecce, D.; Brutti, S.; Panero, S.; Hassoun, J. A New Sn-C/LiFe0.1Co0.9PO4 Full Lithium-Ion Cell with Ionic Liquid-Based Electrolyte. *Mater. Lett.***2014**, *139*, 329–332.

(8) Agostini, M.; Brutti, S.; Hassoun, J. High Voltage Li-Ion Battery Using Exfoliated Graphite/Graphene Nanosheets Anode. *ACS Appl. Mater. Interfaces***2016**, *8* (17), 10850–10857.

(9) Huang, Y.; Lin, Y. C.; Jenkins, D. M.; Chernova, N. A.; Chung, Y.; Radhakrishnan, B.; Chu, I. H.; Fang, J.; Wang, Q.; Omenya, F.; Ong, S. P.; Whittingham, M. S. Thermal Stability and Reactivity of Cathode Materials for Li-Ion Batteries. **2016**, *8* (11), 7013–7021.

(10) El Khakani, S.; Rochefort, D.; MacNeil, D. D. Thermal Stability of High Voltage Li1-xMn1.5Ni0.5O4 Cathode Material Synthesized via a Sol-Gel Method. **2016**, *163* (6), A947–A952.

(11) Martha, S. K.; Haik, O.; Zinigrad, E.; Exnar, I.; Drezen, T.; Miners, J. H.; Aurbach, D. On the Thermal Stability of Olivine Cathode Materials for Lithium-Ion Batteries. **2011**, *158* (10).

(12) Arbizzani, C.; Gabrielli, G.; Mastragostino, M. Thermal Stability and Flammability of

Electrolytes for Lithium-Ion Batteries. *J. Power Sources***2011**, *196* (10), 4801–4805.

(13) Lombardo, L.; Brutti, S.; Assunta, M.; Panero, S.; Reale, P. Mixtures of Ionic Liquid E Alkylcarbonates as Electrolytes for Safe Lithium-Ion Batteries. *J. Power Sources***2013**, *227*, 8–14.

(14) Brutti, S.; Panero, S. Recent Advances in the Development of LiCoPO4 as High Voltage Cathode Material for Li-Ion Batteries. *ACS Symp. Ser.***2013**, *1140*, 67–99.

(15) Brutti, S.; Manzi, J.; De Bonis, A.; Di Lecce, D.; Vitucci, F.; Paolone, A.; Trequattrini, F.; Panero, S. Controlled Synthesis of LiCoPO4 by a Solvo-Thermal Method at 220 °c. *Mater. Lett.***2015**, *145*, 324–327.

(16) Di Lecce, D.; Manzi, J.; Vitucci, F. M.; De Bonis, A.; Panero, S.; Brutti, S. Effect of the Iron Doping in LiCoPO4 Cathode Materials for Lithium Cells. *Electrochim. Acta***2015**, *185*, 17–27.

(17) Boulineau, A.; Gutel, T. Revealing Electrochemically Induced Antisite Defects in LiCoPO4: Evolution upon Cycling. *Chem. Mater.***2015**, *27*, 802–807.

(18) Bramnik, N. N.; Nikolowski, K.; Baehtz, C.; Bramnik, K. G.; Ehrenberg, H. Phase Transitions Occurring upon Lithium Insertion−Extraction of LiCoPO 4. *Chem. Mater.***2007**, *19* (4), 908–915.

(19) Manzi, J.; Vitucci, F. M.; Paolone, A.; Trequattrini, F.; Di Lecce, D.; Panero, S.; Brutti, S. Analysis of the Self-Discharge Process in LiCoPO4 Electrodes: Bulks. *Electrochim. Acta***2015**, *179*, 604–610.

(20) Yoon, W.-S.; Chung, K. Y.; Nam, K.-W.; McBreen, J.; Wang, D.; Huang, X.; Li, H.; Chen, L.; Yang, X.-Q. Electronic Structural Changes of the Electrochemically Delithiated LiFe0.5Co0.5PO4 Cathode Material Studied by X-Ray Absorption Spectroscopy. *J.Power Sources***2008**; *183* (1) 427-430.

(21) Han, D.-W. W.; Kang, Y.-M. M.; Yin, R.-Z. Z.; Song, M.-S. S.; Kwon, H.-S. S. Effects of Fe Doping on the Electrochemical Performance of LiCoPO4/C Composites for High Power-

Density Cathode Materials. *Electrochem. Commun.***2009**, *11* (1), 137–140.

(22) Allen, J. L. L.; Jow, T. R. R.; Wolfenstine, J. Improved Cycle Life of Fe-Substituted LiCoPO4. *J. Power Sources***2011**, *196* (20), 8656–8661.

(23) Kang, Y.-M. M.; Kim, Y.-I. U. J.; Oh, M.-W.; Yin, R.-Z.; Lee, Y.; Han, D.-W.; Kwon, H.-S.; Kim, J. H.; Ramanath, G. Structurally Stabilized Olivine Lithium Phosphate Cathodes with Enhanced Electrochemical Properties through Fe Doping. *Energy Environ. Sci.***2011**, *4* (12), 4978.

(24) Yang, S. M. G.; Aravindan, V.; Cho, W. I.; Chang, D. R.; Kim, H. S.; Lee, Y. S. Realizing the Performance of LiCoPO4 Cathodes by Fe Substitution with Off-Stoichiometry. *J. Electrochem. Soc.***2012**, *159* (7), A1013–A1018.

(25) Strobridge, F. C.; Middlemiss, D. S.; Pell, A. J.; Leskes, M.; Clément, R. J.; Pourpoint, F.; Lu, Z.; Hanna, J. V.; Pintacuda, G.; Emsley, L.; Samoson, A.; Grey, C. P. Characterising Local Environments in High Energy Density Li-Ion Battery Cathodes: A Combined NMR and First Principles Study of LiFe X Co 1−x PO 4. *J. Mater. Chem. A***2014**, *2* (30), 11948.

(26) Kosova, N. V.; Podgornova, O. A.; Devyatkina, E. T.; Podugolnikov, V. R.; Petrov, S. A. Effect of Fe^{2+} Substitution on the Structure and Electrochemistry of $LiCoPO_4$ Prepared by Mechanochemically Assisted Carbothermal Reduction. *J. Mater. Chem. A***2014**, *2* (48), 20697–20705.

(27) Allen, J. L.; Thompson, T.; Sakamoto, J.; Becker, C. R.; Jow, T. R.; Wolfenstine, J. Transport Properties of LiCoPO4 and Fe-Substituted LiCoPO4.**2014**; *254*, 204–208.

(28) Nytén, A.; Thomas, J. O. A Neutron Powder Diffraction Study of LiCoxFe1−xPO4 for x=0, 0.25, 0.40, 0.60 and 0.75. *Solid State Ionics***2006**, *177* (15), 1327–1330.

(29) Wang, D.; Wang, Z.; Huang, X.; Chen, L. Continuous Solid Solutions LiFe1−xCoxPO4 and Its Electrochemical Performance. *J. Power Sources***2005**, *146* (1), 580–583.

(30) Srobridge, F.C.; Liu, H.; Leskes, M.; Borkiewicz, O.J.; Wiaderek, K.M.; Chupas, P.J.; Chapman, K.W.; Grey, C.P. Unravelling the Complexity Delithiation Mechanisms of

Olivine-type Cathode Materials, LiFexCo1-xPO4. *Chem. Mater.***2016**, *28* (11), 3676-3690.

(31) Brutti, S.; Manzi, J.; De Bonis, A.; Di Lecce, D.; Vitucci, F.; Paolone, A. .; Trequattrini, F.; Panero, S. Corrigendum to "Controlled Synthesis of LiCoPO4 by a Solvo-Thermal Method at 220°C" [Mater. Lett. 145 (2015) 324–327]. *Mater. Lett.***2016**, *172*, 98.

(32) Manzi, J.; Curcio, M.; Brutti, S. Structural and Morphological Tuning of LiCoPO4 Materials Synthesized by Solvo-Thermal Methods for Li-Cell Applications. *Nanomaterials***2015**, *5* (4), 2212–2230.

(33) Brutti, S.; Manzi, J.; De Bonis, A.; Di Lecce, D.; Vitucci, F.; Paolone, A. .; Trequattrini, F.; Panero, S. Corrigendum to "Controlled Synthesis of LiCoPO4 by a Solvo-Thermal Method at 220°C" [Mater. Lett. 145 (2015) 324–327]. *Mater. Lett.***2016**, *172*, 98.

(34) Larson, A., Von, R., D. *General Structure Analysis System (GSAS) Los Alamos National Laboratory Report LAUR 86*; 2000.

(35) Brutti, S.; Panero, S. Recent Advances in the Development of LiCoPO4 as High Voltage Cathode Material for Li-Ion Batteries. *ACS Symp. Ser.***2013**, *1140*, 67–99.

(36) Klementev, K. V. Extraction of the Fine Structure from X-Ray Absorption Spectra. *J. Phys. D. Appl. Phys.***2001**, *34* (2), 209–217.

(37) Ravel, B.; Newville, M.; et al. *ATHENA* , *ARTEMIS* , *HEPHAESTUS* : Data Analysis for X-Ray Absorption Spectroscopy Using *IFEFFIT*. *J. Synchrotron Radiat.***2005**, *12* (4), 537–541.

(38) Di Lecce, D.; Hassoun, J. Lithium Transport Properties in $LiMn_{1-\alpha}Fe_{\alpha}PO_4$ Olivine Cathodes. *J. Phys. Chem. C***2015**, *119* (36), 20855–20863.

(39) Snyder, R.L., Bish, D. L. Quantitative Analysis, Rev. Mineral. *Geochemistry***1989**, *20*, 101–144.

(40) Kandhasamy, S.; Nallathamby, K.; Minakshi, M. Role of Structural Defects in Olivine Cathodes. *Prog. Solid State Chem.***2012**, *40* (1–2), 1–5.

(41) Shannon, R. D. Revised Effective Ionic Radii and Systematic Studies of Interatomie Distances in Halides and Chaleogenides.*Acta Cryst.***1976**, *A32*, 751-767

(42) Farges, F; Ponader, C.W.; Brown, G. E. J. Structural environments of incompatible elements in silicate glass/melt systems: I. Zirconium at trace levels. *Geochim. Cosmochim. Acta***1991**, *55*, 1563.

(43) Deb, A.; Bergmann, U.; Cramer, S. P.; Cairns, E. J. Structural Investigations of LiFePO4 Electrodes and in Situ Studies by Fe X-Ray Absorption Spectroscopy. *Electrochim. Acta***2005**, *50* (25), 5200–5207.

(44) Haas, O.; Deb, A.; Cairns, E. J.; Wokaun, A. Synchrotron X-Ray Absorption Study of LiFePO[sub 4] Electrodes. *J. Electrochem. Soc.***2005**, *152* (1), A191.

(45) Kang, Y.-M.; Kim, Y.-I.; Oh, M.-W.; Yin, R.-Z.; Lee, Y.; Han, D.-W.; Kwon, H.-S.; Kim, J. H.; Ramanath. Structurally Stabilized Olivine Lithium Phosphate Cathodes with Enhanced Electrochemical Properties through Fe Doping. *Energy Environ. Sci.***2011**, *4* (12), 4978.

(46) Zhao, T.; Chu, W.; Zhao, H.; Liang, X.; Xu, W.; Yu, M.; Xia, D.; Wu, Z. XAS Study of LiFePO4 Synthesized by Solid State Reactions and Hydrothermal Method. *Nucl. Instruments Methods Phys. Res. Sect. A Accel. Spectrometers, Detect. Assoc. Equip.***2010**, *619* (1), 122–127.

(47) Islam, M. S.; Driscoll, D. J.; Fisher, C. A. J.; Slater, P. R.; Group, M. C.; V, C. Di; Uni, V.; Gu, G.; Kingdom, U. Atomic-Scale Investigation of Defects , Dopants , and Lithium Transport in the LiFePO 4 Olivine-Type Battery Material. **2005**, No. 11, 5085–5092.

(48) Ouyang, C.; Shi, S.; Wang, Z.; Huang, X.; Chen, L. First-Principles Study of Li Ion Diffusion in LiFePO4. *Phys. Rev. B***2004**, *69* (10), 104303.

(49) Fisher, C. A. J.; Hart Prieto, V. M.; Islam, M. S. Lithium Battery Materials Li *M* PO $_4$ (*M* = Mn, Fe, Co, and Ni): Insights into Defect Association, Transport Mechanisms, and Doping Behavior. *Chem. Mater.***2008**, *20* (18), 5907–5915.